ACS OMEGA

http://pubs.acs.org/journal/acsodf

Article

Biosafety, Nontoxic Nanoparticles for VL−NIR Photothermal Therapy Against Oral Squamous Cell Carcinoma

Jinhuan Chen, Qionghua Li, Fei Wang, Ming Yang,* Liang Xie,* and Xin Zeng*

Cite This: *ACS Omega* 2021, 6, 11240−11247

Read Online

ACCESS | Metrics & More | Article Recommendations | Supporting Information

ABSTRACT: Semiconductor nanocrystals with extraordinary physicochemical and biosafety properties with unique nanostructures have shown tremendous potential as photothermal therapy (PTT) nanosensitizers. Herein, we successfully synthesized chiral molybdenum (Cys-MoO_{3-x}) nanoparticles (NPs) for overcoming the general limitation on electron energy bands and biotoxicity. The obtained Cys-MoO_{3-x} NPs are selected as an ideal design for the treatment of oral squamous cell carcinoma (OSCC) cells through the decoration of cysteine molecules due to excellent initial photothermal spectral analysis of conductivity and light absorbance. Notably, NPs possess the ability to act as visible light (VL) and near-infrared (NIR) double-reactive agents to ablate cancer cells. By combining photoconductive PTT with hypotoxicity biochemotherapy, the treatment validity of OSCC cancer cells can be improved in vitro by up to 89% (808 nm) and get potential PTT effect under VL irradiation, which intuitively proved that the nontoxic NPs were lethally effective for cancer cells under laser irradiation. Hence, this work highlights a powerful and safe NP platform for NIR light-triggered PTT for use in head and neck cancer (HNC) cells, showing promising application prospects in oral tumor treatment.

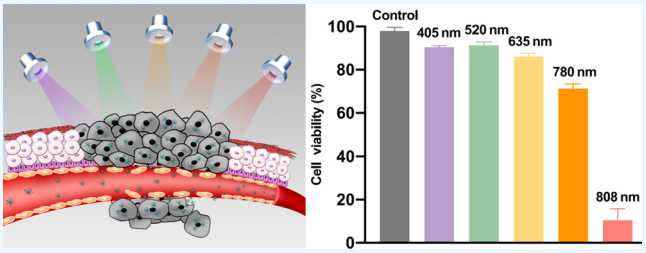

INTRODUCTION

Head and neck cancer (HNC) is one of the most catastrophic malignant tumors affecting patients' quality of life due to its frequent lymphatic metastasis, relatively low response to treatment, and severe drug resistance.[1−3] Oral squamous cell carcinoma (OSCC) accounts for the vast majority of HNC cases, and there are a few noninvasive, biosafety, and effective treatments.[4−6] Photothermal therapy (PTT), as a strategy for treating these cancers in combination with a noninvasive method has the advantage of being safe and efficient and is poised to be used as an adjuvant therapy to traditional-simplex surgical excision procedures where patients who do survive would be left with severe facial and visceral defects.[7−10] PTT is the local heating of tumor cells using light radiation and systemic local spot hyperthermia, causing irreversible damage of tumor cells through protein denaturation and cell membrane rupture.[11,12]

Research on PTT is still growing and has achieved good results in many fields.[13−18] In tumor oncology, PTT is an artificial photosensitizer that is used to increase the local-tissue temperature of the intolerance target cells to achieve tumor cell apoptosis or necrosis.[19,20] The excitation source of a PTT reagent (metal nanoparticles (NPs) and carbon-based nanomaterials) is usually near-infrared (NIR) light, which possesses high penetration efficiency to the human body and often needs complicated synthetic processes.[21−30] Despite the remarkable development of PTT technology, it is still difficult to achieve a balance between the effective stimulation of tumor cell death by high-penetration laser and reducing the damage to adjacent normal tissues by low radiation due to the use of materials for near-infrared absorption. Besides, many nanomaterials have crucial defects with biodegradation and excretion in the physiological environment due to their crystallinity with few defects that limit their in vivo application.[31−33] Meta-analysis studies on a large scale of NP delivery point out that over 99% of the applied dose of the nanomedicine cannot eventually accumulate in the tumor and some even remain in the body for over 2 years.[34,35] In addition to the medical effectiveness of PTT, the long-term safety of photothermic agents (PTAs) must also be considered.[36−39] Therefore, molybdenum (MoO_{3-x}) NPs have attracted extensive attention in recent years due to their large optical adsorption coefficient and biocompatibility and their tunable adsorption performance in the extreme NIR range. Despite the excellent photothermal transductant, its insolubility is the limit of semplice MoO_{3-x} PTT usage.[40−44]

We improve the uptake of NPs into tumor cells through linking up with well-soluble cysteine, without compromising its

Received: January 7, 2021
Accepted: April 6, 2021
Published: April 19, 2021

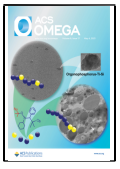

ACS Publications

© 2021 The Authors. Published by American Chemical Society

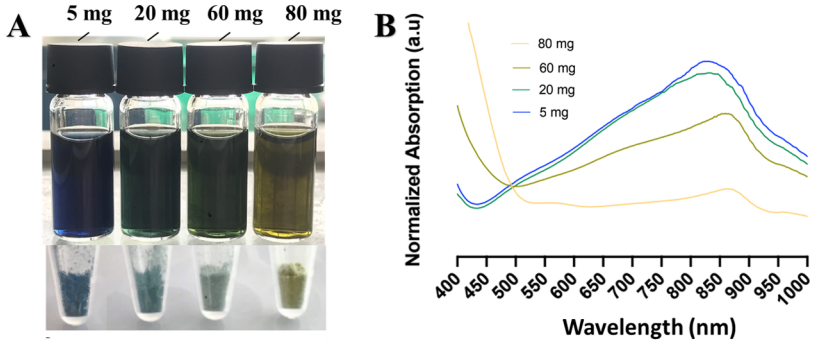

Figure 1. (A) Synthesis of MoO_{3-x} NPs with different contents of cysteine (5, 20, 60, and 80 mg). Final solutions (upper portion) and the material powder (lower portion) appear in different colors due to different valences of Mo (Mo molality: 10×10^{-3} M). (B) VL−NIR region absorption spectra of the four different valence Cys-MoO_{3-x} states.

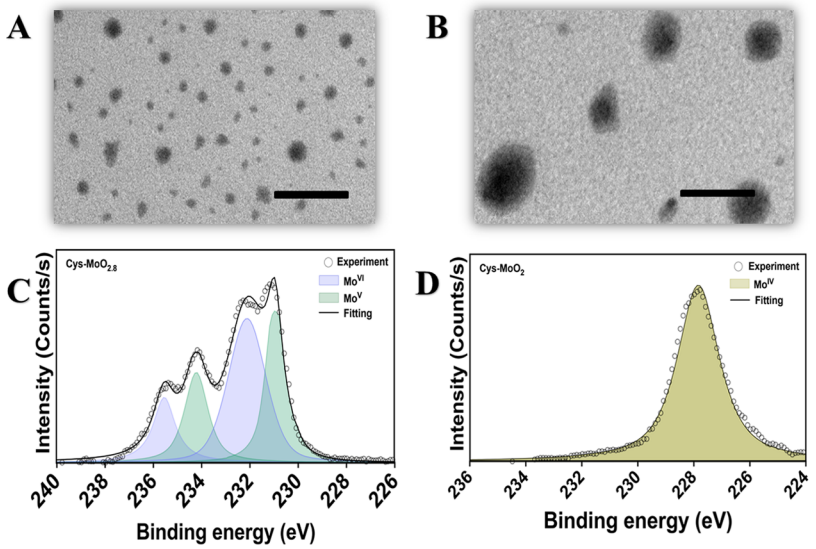

Figure 2. (A, B) TEM morphology characterizations of Cys-MoO_{3-x} NPs. TEM images of the prepared Cys-MoO_{3-x} NPs with different colors; scale bar: 50 nm. (C, D) Typical X-ray photoelectron spectroscopy (XPS) measurements of the prepared NPs with different valence states related to (A) and (B) above.

optical performance.[45] Hence, we successfully prepared MoO_{3-x} NPs, which have the advantages of nontoxicity and biodegradation ability. After studying the optical properties, we further optimized the selected "Cys-MoO_{3-x}" NPs to be applied in the typical HNC culprit OSCC cells for biosafety purposes and achieved multicertification to prove their lethal action from 405 to 808 nm laser. We verified and synthesized their biosafety and therapeutic effects in in vivo experiments, including their optical performance, photothermal conductivity, and biosafety analysis. Finally, we applied them to OSCC cells and found that they had a visible light (VL) to NIR dual PTT effect, with tumor cell fatality rates up to 89%. The derivative application of MoO_{3-x} NPs will further promote the treatment of PTT against HNC.

RESULTS AND DISCUSSION

Cys-MoO_{3-x} NPs can target tumor cells by enhanced permeability, retention, active endocytosis, and exploit the PTT process with both VL and NIR radiation, while the excess nanomedicine is eliminated in a quick and safe way by renal excretion. Then, we investigated the light absorption of different masses of cysteine on the synthesis of MoO_{3-x} NPs by gradually adding 5, 20, 60, and 80 mg of cysteine into the Mo solution with a same molal concentration (10×10^{-3} M). The resulting solution is shown in blue, dark green, light green, and dark yellow in Figure 1A. The color difference is that the Mo valence of the sample is different due to the addition of different contents of cysteine.[46] Figure 1B shows the very different transition of the absorption bands of these samples. It is obvious that the blue group has the highest light absorption in the NIR region and the yellow group matches the VL region. But no comparative advantage of the other two green samples was seen. So, the initial screening of further experiments goes to 5 and 80 mg groups.

The transmission electron microscopy (TEM) morphology characterization of MoO_{3-x} NPs with 5 and 80 mg of cysteine is shown in Figure 2A,B. The particles of MoO_{3-x} NP samples prepared are approximately spherical. The diameter of the blue sample is nearly 5 nm (Figure 2A), while the yellow sample reaches over 30 nm (Figure 2B). Actually, the diameters of MoO_{3-x} NP particles increase with the change in the color and their corresponding Mo valences (Figures S1 and S2).

X-ray surface photoelectron spectroscopy (XPS) is carried out to analyze the actual molybdenum valence states of these NPs. As shown in Figure 2C,D, by analyzing the peak area ratio, we calculate the proportion of the NP component of the

https://doi.org/10.1021/acsomega.1c00101
ACS Omega 2021, 6, 11240−11247

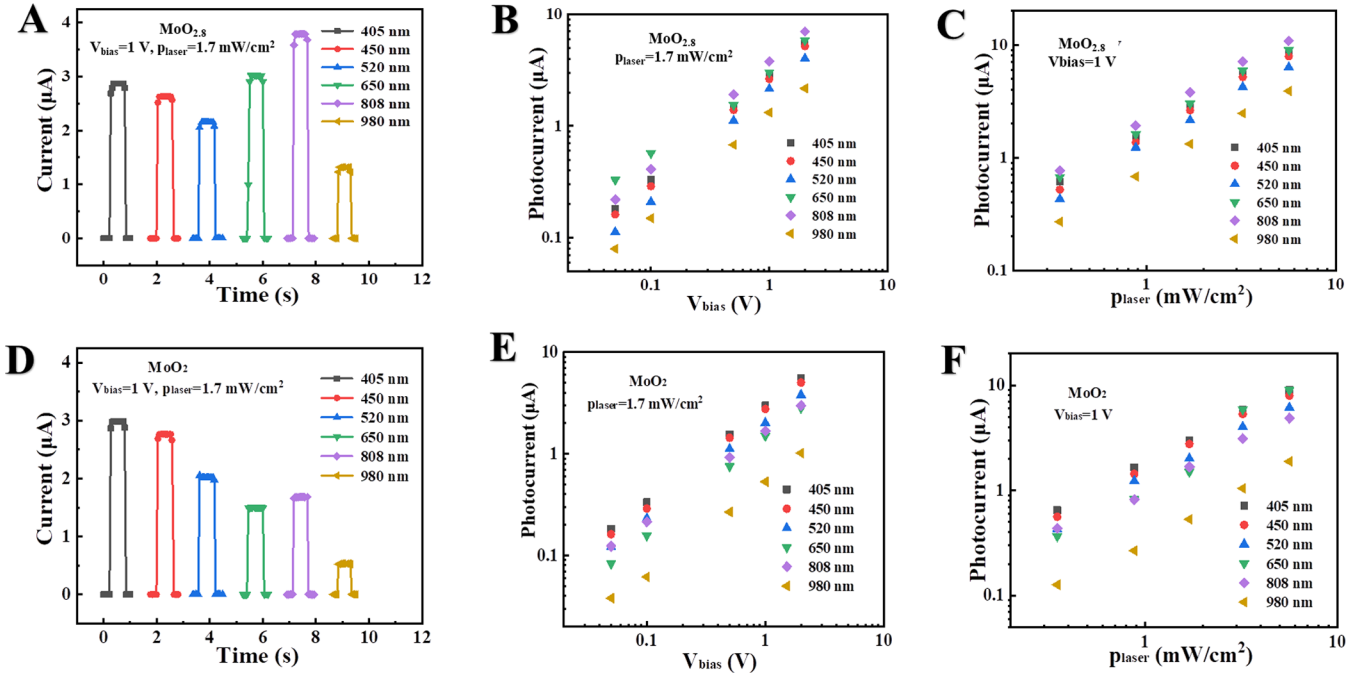

Figure 3. Optoelectronic property of Cys-MoO_{3-x} NPs. (A, D) I_{ph} curves of Cys-$MoO_{2.8}$ NP and Cys-MoO_2 NP devices under light irradiation with different wavebands (405−980 nm at V_{bias} = 1 V with an irradiation power intensity of 1.7 mW cm^{-2}. (B, E) I_{ph} curves of Cys-$MoO_{2.8}$ NP and Cys-MoO_2 NP devices at different V_{bias} values with a laser power intensity of 1.7 mW cm^{-2}. (C, F) I_{ph} curves of Cys-$MoO_{2.8}$ NP and Cys-MoO_2 NP devices under different laser power densities, when V_{bias} = 1 V.

mixing valence between Mo^{IV} and $Mo^{VI}$by determining the mixed valence state of the blue sample (5 mg) under a slightest reduction that turned to be $MoO_{2.8}$. The dark yellow one under the strongest reduction (80 mg) was MoO_2. Two other green samples under moderate reduction were $MoO_{2.11}$ and $MoO_{2.03}$ (Figures 3 and S4). The above XPS results indicated that the successful switching band between the valence states of Mo and MLCT depended on the concentration of cysteine, which provided a platform for further VL−NIR thermal activity experiments.[47]

We tested the dynamic light scattering (DLS) of the four nanoparticle solutions and also the semifinished product, MoO_3 (Figures S5 and S6); it turned out that as MoO_{3-x} was wrapped and reduced by more amount of cysteine,[49,50] the hydrodynamic diameter increased gradually from 293.1 to 449.6 nm with uniform distribution. MoO_3 in the absence of cysteine has a DLS size of 269.9 nm.

To analyze the structural information of the samples, we also performed X-ray diffraction (XRD) study and thermogravimetric analysis (TGA). As shown in Figure S7A, XRD tests revealed the structure of our samples with MoO_{3-x} content. With the increase of the concentration of cysteine, the reduction degree of the molybdenum oxide increases and the XRD pattern shows more image composition of cysteine.[48,49] According to Figure S7B, we estimated that the weight loss of cysteine content occurred in the second and third curves, that is, for $MoO_{2.8}$, $MoO_{2.11}$, $MoO_{2.03}$, and MoO_2 NPs; the amino acid contents were calculated to be 10.38, 10.89, 11.78, and 17.95%, respectively.

Next, we focus our attention on Cys-$MoO_{2.8}$ and Cys-MoO_2 that have highest absorptions at wavelengths of 808 and 405 nm, respectively. We prepared Cys-$MoO_{2.4}$ and Cys-MoO_2 NPs by drip-coating on Si/SiO_2 with a Au electrode and tested them (Figure S8); we then studied their photoelectric transduction properties. Under illumination with different wavelengths, I_{ph}'s of Cys-$MoO_{2.8}$ and Cys-MoO_2 NPs show a broad-band response from the VL to NIR region and an outstanding photoresponse. Broad-band wavelength pulse lasers served as the photoelectric properties of the Cys-$MoO_{2.8}$ NP and Cys-MoO_2 NP devices, displaying switching performance between on and off conduction states (Figure 3A,D). I_{ph} is linearly dependent on the bias voltage (V_{bias}) at both ends of the device (Figure 3B,E) and the laser power density (Figure 3C,F). With V_{bias} increasing from 0.05 to 2 V, I_{ph} of the Cys-$MoO_{2.8}$ NP device (@808 nm) increases from 216 nA to 7.1 μA with an irradiation power density of 1.7 mW cm^{-2}. Meanwhile, I_{ph} of the Cys-MoO_2 NP device (@405 nm) increases from 651 nA to 9 μA under the same conditions. When laser irradiation power increases from 0.27 to 6.07 mW cm^{-2}, I_{ph} of the Cys-$MoO_{2.8}$ NP device (@808 nm) and the Cys-MoO_2 NP device (@405 nm) linearly increases by 34 and 31 times at V_{bias} = 1 V, respectively. So, the Cys-$MoO_{2.8}$ NP and Cys-MoO_2 NP devices have distinguished stabilities and linear photoelectric detection capabilities. For Cys-$MoO_{2.8}$ NPs@808 nm and Cys-MoO_2 NPs@405, I_{ph} generation is the maximum, indicating the basis for the subsequent application of PTT. It also indicates the potential of the Cys-$MoO_{2.8}$ NPs and Cys-MoO_2NPs prepared in the experiment to be applied in the VL to NIR region. The optical detection method complies with the temperature change described in Figure S9A and the photostability test of Cys-$MoO_{2.8}$ in Figure S9B.

NIR (780−1100 nm) photons are known to have a greater biotissue-transparency capacity when compared with shorter wavelength light.[50−52] With the cross section of optimized photoelectric properties at around 800 nm, Cys-$MoO_{2.8}$ can serve as an ideal PTA for clinical treatment. The MoO_{3-x} surface modified by the zwitterionic cysteine vastly improved

https://doi.org/10.1021/acsomega.1c00101
ACS Omega 2021, 6, 11240−11247

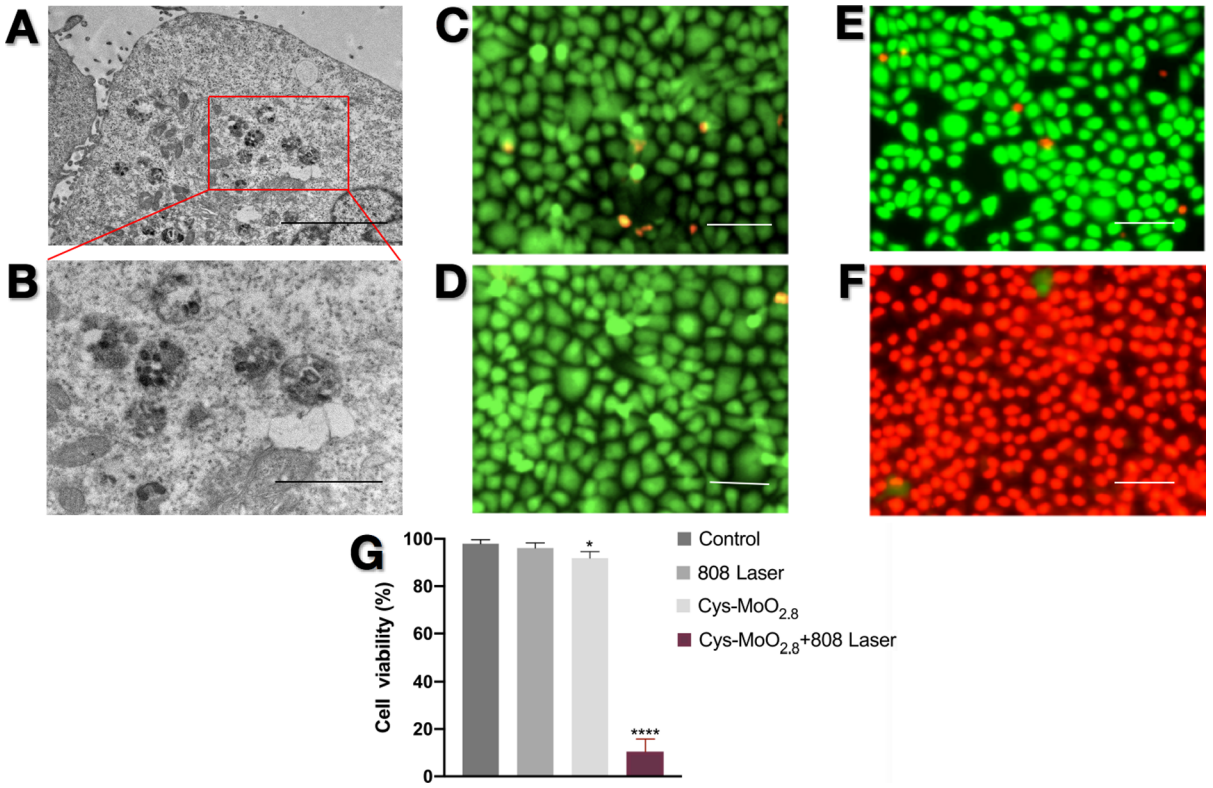

Figure 4. (A/B) Bio-TEM images of the OSCC cell morphology 24 h after adding Cys-$MoO_{2.8}$ NPs. Scale bar: (A) 500 nm and (B) 200 nm. (C−F) Live/dead cells, scale bar: 50 μm, (C) blank control, (D) cell cultured with only laser but no NPs, (E) cell cultured with Cys-$MoO_{2.8}$ NPs, (F) cells cultured with Cys-$MoO_{2.8}$ NPs and 808 laser, and (G) cell viability of OSCC cells + Cys-$MoO_{2.8}$ NPs with/without 808 laser was analyzed by the CCK-8 assay.

the solubility and optical ability. A recent metabolism experiment of MoO_{3-x} NPs detected very high concentrations of Mo ions in the urine sample collected and confirmed that up to 50% of Mo elements were eliminated in the urine quickly.[53] Based on PTT optimization, we used Cys-$MoO_{2.8}$ in the in vitro OSCC experiment.

As shown in Figure 4A,B, the bio-TEM image confirms the typical uptake of Cys-$MoO_{2.8}$ NPs by cell endocytosis with no significant cellular damage. The membrane structure remains intact and the cytoplasm is uniform with no morphological changes. A magnified image in Figure 4B clearly shows that the cell membrane is wrapping off the NPs followed by cellular uptake on its own initiative. The Cys-MoO_{3-x} NPs may aggregate into small clusters through membrane curvature-mediated attraction in the cytoplasm, and therefore be able to be internalize together.[54] After crossing the cellular membrane, the NP clusters were still clearly visible.

After validating the cell morphology and intake of the targeting NPs, we begin irradiating the 24 h "Cys-$MoO_{2.8}$" cultured cells with a 808 nm laser. The CCK-8 cell viability assay counts are shown in Figure 4G. Cell groups with either laser exposure or Cys-$MoO_{2.8}$ absorption showed, respectively, 96 and 91% of the cells to be viable. The latter may due to the small amount of NP sediment obstructing bits of cell attachment. The group with Cys-$MoO_{2.8}$ NPs exposed to a 808 nm laser reached the lowest survival cell rate of 11%. Further confirmation of specific cell death was proved by calcein-acetoxymethyl (AM)/propidium iodide (PI) cell staining. The virtually cell-permeant and nonfluorescent neutral dye can be converted by living cell esterases into its negative analogue with an impermeant green fluorescence. This intense green fluorescence dye is well retained in viable OSCC cells, while propidium iodide PI enters cells featured with membrane degradation or deficiency, a character of late apoptosis or necrosis, and react with nucleic acid that significantly amplifies the red fluorescence. Figure 4C−F shows the test groups in Figure 4G. Neither Figure 4D,E for cell cultured with a single component of a 808 nm laser and Cys-$MoO_{2.8}$ shows difference with the control group (Figure 4C), which are not only sparsely but evenly distributed dead signals; all of these facts are conformable to the calculated CCK-8 results. Meanwhile, in the local irradiation area, as the temperature increased rapidly in Cys-$MoO_{2.8}$ NPs with a 808 nm laser group (Figure 4F), massive cell death occurs. The adherent cells were charred and dyed red at the dish bottom because of the rapid increase in the temperature, which proved to be ocular proof of the PTT effect of selected Cys-MoO_{3-x} NPs and optimum light wavelength on OSCC cells.

We change the laser wavelengths while other conditions remain the same to test the VL−NIR photodetection of Cys-MoO_{3-x}. The results are shown in Figure 5G. Cell viability under 780 nm laser irradiation remains 71 and 86% for the 603 nm group but the photothermal effect at 520 and 405 nm has no statistical positivity with the control group. Figure 5A−F shows the live/dead staining of cell groups in Figure 4G, focusing on the irradiation area. It can be seen clearly that from 405 to 808 nm, with the increase in the laser wavelength, the cell dying ratio due to PTT therapy increases.

For a positive control, we immerse OSCC cells in different temperature environments and directly measure the proportions of viable cells. When exposed to temperatures above 45 °C for 20 min, cell viability statistically decreased and when

https://doi.org/10.1021/acsomega.1c00101
ACS Omega 2021, 6, 11240−11247

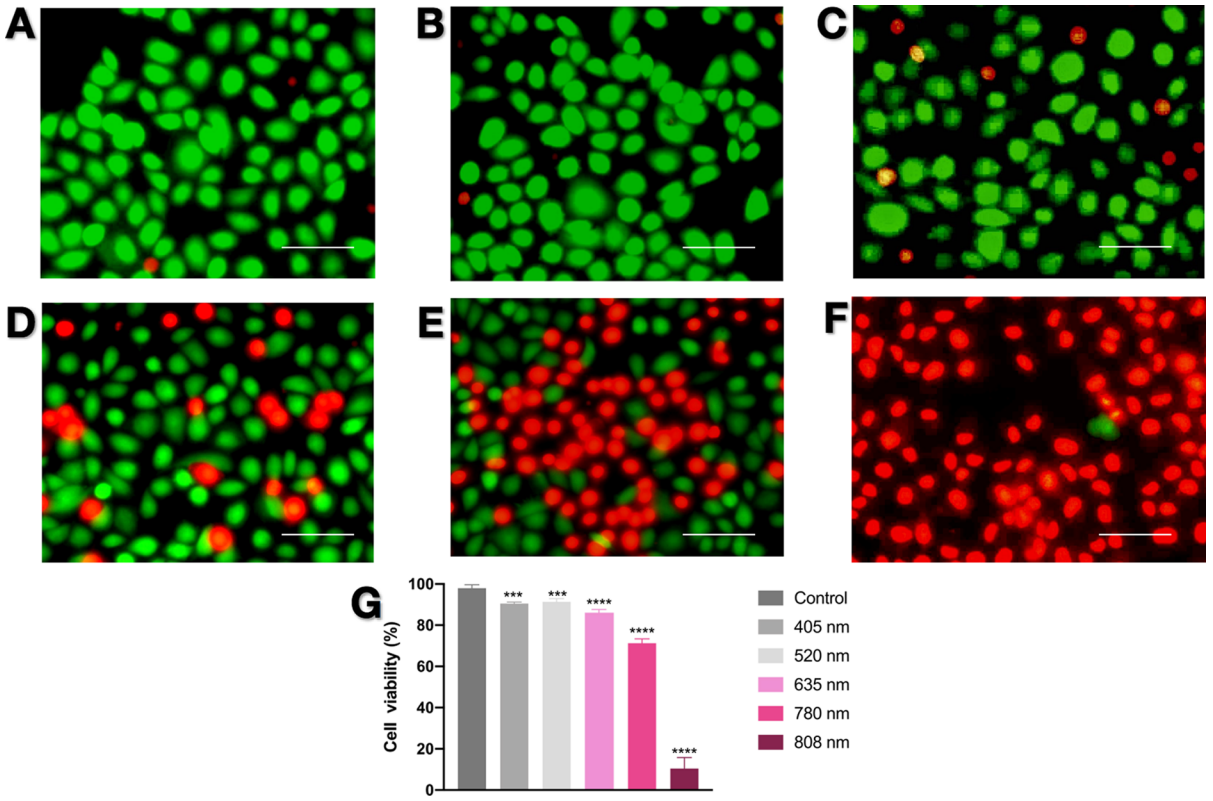

Figure 5. (A–F) Live/dead staining images of NP cultured cells after irradiation by different wavelengths of laser are, in turn, (A) blank control, (B) for 405 nm, (C) for 520 nm, (D) for 630 nm, (E) for 780 nm, and (F) for 808 nm. Scale bar: 50 μm. (G) Cell viability after laser irradiation at different wavelengths.

gradually warmed up to 60 °C, rare cells were alive. The PTT lethal effect on OSCC cells under different wavelengths of the laser matches perfectly with our optical observation on Cys-$MoO_{2.8}$. This also reflects that our cysteine-wrapping MoO_{3-x} maintains the original outstanding optical properties after increasing its solubility. We recommend a 808 nm laser in future in vivo study.

The well-advised 808 nm light maximizes light–nanomaterial interactions of Cys-$MoO_{2.8}$. It guarantees effective and selective hyperthermia, which causes lethal damages to OSCC cells by cell necrosis. OSCC usually occurs on the dorsal, ventral of the tongue, and mouth floor, or secondary to oral mucosal carcinoma in situ and mucosal precancerous lesions. The specially developed anatomic sites made it possible and meaningful for local treatment Cys-MoO_{3-x} application. The exposition of multipoint 808 nm laser and application of irradiation of different wavelengths may enhance and precisely control the penetrating depth and targeting section.

CONCLUSIONS

The Cys-MoO_{3-x} NPs with remarkable photoelectric properties could reshape the PTA detection mode and provide a platform for further application of more PTT cancer therapy. The cytotoxicity of Cys-MoO_{3-x} NPs is evaluated in vitro study by cytoactive assay and bio-TEM cellular examination. We investigated the therapeutic efficiency of NPs on OSCC cells under linear light irradiation. Both NIR (808 nm) and VL (405 nm) photothermal efficiency and the fatality rate increases in PTT performance, which could prove Cys-MoO_{3-x} NPs to be a sensitive PTT for OSCC tumor cell ablation. Furthermore, the VL and NIR response for the dual-responsive PTT agent not only provides an integrated efficient photodetection method but also reaches the balance of drug-efficient deposition and surgical precision photothermal therapy (Figure S10). Actually, we had primarily verified Cys-MoO_{3-x} NPs in vivo safety in the further animal experiment and went on the effectiveness research studies in order (L). Hence, restoring MoO_{3-x} to its anoxic state provides versatile possibilities for MoO_3 NP surface modification, giving them preferable biocompatible and physical properties in typical single-pot synthesis.

EXPERIMENTAL SECTION

Materials. Molybdenum sulfide and L-cysteine were obtained from Sigma-Aldrich (St. Louis, MO) and H_2O_2 was obtained from JinShan Chemical Test (China). All other chemicals were available from J&K Chemicals (Beijing, China). OSCC cells were obtained from the JCRB Cell Bank (NIBIOHN, Japan).[55] Eighty milligrams of the pristine MoS_2 powder was dissolved in a mixture of 46.25 mL of deionized (DI) water and 3.75 mL of 30 wt % H_2O_2. The mixture was stirred well till it became black and the MoS_2 powder completely dissolved and the overall solution turned transparent yellow. Then, it was heated up to 80 °C for 1 h to remove excess H_2O_2. Next, 5, 20, 60, and 80 mg of L-cysteine were added as four experimental groups into 1.5 mL of the as-prepared solution to obtain Cys-MoO_{3-x} NPs with increasingly reductant Mo valence states,. The products were sonicated, dissolved, and kept in the dark before use.

Characterization. The morphologies of varying degrees of reduced Cys-MoO_{3-x} were examined using transmission electron microscopy (TEM, JEOL-1200). The UV–vis

https://doi.org/10.1021/acsomega.1c00101
ACS Omega 2021, 6, 11240–11247

absorption spectra of the experimental Cys-MoO_{3-x} groups were recorded using a spectrophotometer (Thermo Variskan LUX). Then, the different Mo valence states in compounds determined by XPS spectra point out the specific value in further calculation. A Bruker AXS D8 Advance was used for XRD analysis. The photoelectric performances (I_{ph} of Cys-MoO_{3-x} NPs) were tested using a sourcemeter (Keithley 2636B) at normal temperatures and pressures. Dynamic light scattering was analyzed using a (Malvern) Zetasizer Nano S90. A (DSC/DTA-TGSTA) 449 F3 Jupiter was used for thermogravimetric analysis (TGA).

Bio-TEM. To observe the cell uptake path of Cys-MoO_{3-x} NPs, 10^6 cells were seeded per 10 cm plates 24 h before the experiment. Cys-MoO_{3-x} NPs were then added into the cultured medium with OSCC cells. After 24 h of incubation, the cell samples were imaged using a JEOL-1200 (Japan).

PTT Effect on OSCC Cells. Cells were cultured in a Dulbecco's modified Eagle medium (DMEM) medium (HyClone SH30022.01B) containing 10% fetal bovine serum (FBS) (Gibco) and 1% penicillin−streptomycin (Sigma). We optimized the concentration of Cys-$MoO_{2.8}$ in the culture of tumor cells to 10^{-3} M for the Mo element. Cells were seeded in 96-well plates at 10^4 cells each 1 day in advance. Then, we refreshed the medium with 10^{-3} M Cys-$MoO_{2.8}$ and cultured for another 24 h. Then, it was irradiated with 405−808 nm laser at 1 W cm^{-2} to Cys-$MoO_{2.8}$ for 20 min each well.

Cell Viability Assay. The cell counting kit-8 (Dojindo CK04, Japan) was used to calculate the cell surviving rate after PTT. Briefly, after PTT, the medium was changed with a 90 mL mixture of a fresh medium and 10 mL of the cell counting kit solution. After 1 h of incubation at 37°C, we read the plate at 450 nm using a microplate reader (Thermo Variskan LUX). The cell surviving rate was determined by the OD experiment/OD blank medium ratio.

Live/Dead Assay. To clearly visualize the live and dead cells, we used the calcein-AM/PI Double Staining Kit (Dojindo C542, Japan) according to the manufacturer's instructions, and cell images were imaged using the Olympus IX71 (Tokyo, Japan) microscope.

Statistical Analysis. Presented research data were replicated three times. One-way analysis of variance (ANOVA) or two-tailed independent test was used for statistical analysis. All results were processed as the mean standard deviation.

■ ASSOCIATED CONTENT

Supporting Information

The Supporting Information is available free of charge at https://pubs.acs.org/doi/10.1021/acsomega.1c00101.

TEM images of the dark blue sample, Cys-$MoO_{2.11}$ NPs and Cys-$MoO_{2.03}$ NPs, XPS measurements of Cys-MoO_{3-x}, and the schematic diagram of the Cys-MoO_{3-x} NP device (PDF)

■ AUTHOR INFORMATION

Corresponding Authors

Ming Yang − *School of Optoelectronic Science and Engineering, University of Electronic Science and Technology of China, Chengdu 610054, P. R. China*; Email: yangming932@163.com

Liang Xie − *State Key Laboratory of Oral Diseases, National Clinical Research Center for Oral Diseases, Chinese Academy of Medical Sciences Research Unit of Oral Carcinogenesis and Management, West China Hospital of Stomatology, Sichuan University, Chengdu 610041, P. R. China*; Email: lxie@scu.edu.cn

Xin Zeng − *State Key Laboratory of Oral Diseases, National Clinical Research Center for Oral Diseases, Chinese Academy of Medical Sciences Research Unit of Oral Carcinogenesis and Management, West China Hospital of Stomatology, Sichuan University, Chengdu 610041, P. R. China*; orcid.org/0000-0002-9590-359X; Email: zengxin22@163.com

Authors

Jinhuan Chen − *State Key Laboratory of Oral Diseases, National Clinical Research Center for Oral Diseases, Chinese Academy of Medical Sciences Research Unit of Oral Carcinogenesis and Management, West China Hospital of Stomatology, Sichuan University, Chengdu 610041, P. R. China*

Qionghua Li − *State Key Laboratory of Oral Diseases, National Clinical Research Center for Oral Diseases, Chinese Academy of Medical Sciences Research Unit of Oral Carcinogenesis and Management, West China Hospital of Stomatology, Sichuan University, Chengdu 610041, P. R. China*

Fei Wang − *State Key Laboratory of Oral Diseases, National Clinical Research Center for Oral Diseases, Chinese Academy of Medical Sciences Research Unit of Oral Carcinogenesis and Management, West China Hospital of Stomatology, Sichuan University, Chengdu 610041, P. R. China*

Complete contact information is available at: https://pubs.acs.org/10.1021/acsomega.1c00101

Author Contributions

J.C. conducted experimental measurement. F.W. analyzed the data. Q.L. polished the article. X.Z, L.X., and M.Y. provided suggestions and assistance to this experiment. All authors discussed the experimental results.

Notes

The authors declare no competing financial interest.

■ ACKNOWLEDGMENTS

This work was supported by the National Natural Science Foundation of China (Nos. U19A2005, 82071137, and 81771081), the CAMS Innovation Fund for Medical Sciences (CIFMS) (2019-12M-5-004 and 2020-I2M-C&T-A-023), and the Sichuan Science and Technology Program (Grant Nos. 2020JDRC0061 and 2020YJ0286).

■ REFERENCES

(1) Chow, L. Q. M. Head and neck cancer. *N. Engl. J. Med.* **2020**, *382*, 60−72.

(2) Siegel, R. L.; Miller, K. D.; Jemal, A. Cancer statistics 2018. *Ca-Cancer J. Clin.* **2018**, *68*, 7−30.

(3) Cramer, J. D.; Burtness, B.; Le, Q. T.; Ferris, R. L. The changing therapeutic landscape of head and neck cancer. *Nat. Rev. Clin. Oncol.* **2019**, *16*, 669−683.

(4) Peltanova, B.; Raudenska, M.; Masarik, M. Effect of tumor microenvironment on pathogenesis of the head and neck squamous cell carcinoma: a systematic review. *Mol. Cancer* **2019**, *18*, 63−86.

(5) Bray, F.; Ferlay, J.; Soerjomataram, I.; Siegel, R. L.; Torre, L. A.; Jemal, A. Global cancer statistics 2018: GLOBOCAN estimates of incidence and mortality worldwide for 36 cancers in 185 countries. *Ca-Cancer J. Clin.* **2018**, *68*, 394−424.

(6) Wyss, A.; Hashibe, M.; Chuang, S. C.; et al. Cigarette, cigar, and pipe smoking and the risk of head and neck cancers: pooled analysis in the International Head and Neck Cancer Epidemiology Consortium. *Am. J. Epidemiol.* **2013**, *178*, 679−690.
(7) Brockstein, B.; Haraf, D. J.; Rademaker, A. W.; Kies, M. S.; Stenson, K. M.; Rosen, F.; Mittal, B. B.; Pelzer, H.; Fung, B. B.; Witt, M.-E.; Wenig, B.; Portugal, L.; Weichselbaum, R. W.; Vokes, E. E. Patterns of failure, prognostic factors and survival in locoregionally advanced head and neck cancer treated with concomitant chemo-radiotherapy: a 9-year, 337-patient, multi-institutional experience. *Ann. Oncol.* **2004**, *15*, 1179−1186.
(8) Braakhuis, B. J. M.; Brakenhoff, R. H.; Leemans, C. R. Treatment choice for locally advanced head and neck cancers on the basis of risk factors: biological risk factors. *Ann. Oncol.* **2012**, *23*, x173−x177.
(9) Lefebvre, J. L. Current clinical outcomes demand new treatment options for SCCHN. *Ann. Oncol.* **2005**, *16*, vi7−vi12.
(10) Cohen, E. E. W.; LaMonte, S. J.; Erb, N. L.; Beckman, K. L.; Sadeghi, N.; Hutcheson, K. A.; Stubblefield, M. D.; Abbott, D. M.; Fisher, P. S.; Stein, K. D.; Lyman, G. H. American Cancer Society Head and Neck Cancer Survivorship Care Guideline. *Ca-Cancer J. Clin.* **2016**, *66*, 203−239.
(11) Huang, D. Y.; Hou, Y. L.; Yang, S. M.; Wang, R. G. Advances in Nanomedicine for Head and neck cancer. *Front. Biosci.* **2014**, *19*, 783−788.
(12) Dickerson, E. B.; Dreaden, E. C.; Huang, X. H.; El-Sayed, I. H.; Chu, H. H.; Pushpanketh, S.; McDonald, J. F.; El-Sayed, M. A. Gold nanorod assisted near-infrared plasmonic photothermal therapy (PPTT) of squamous cell carcinoma in mice. *Cancer Lett.* **2008**, *269*, 57−66.
(13) Hou, X. Y.; Tao, Y. K.; Pang, Y. Y.; Li, X. X.; Liu, Y. Q.; Jiang, G. Nanoparticle—based photothermal and photodynamic immuno-therapy for tumor treatment. *Int. J. Cancer* **2018**, *143*, 3050−3060.
(14) Xia, D. H.; Liu, H. D.; Xu, B. H.; Wang, Y. C. Single Ag atom engineered 3D-MnO2 porous hollow microspheres for rapid photo-thermocatalytic inactivation of E. coli under solar light. *Appl. Catal., B* **2019**, *245*, 177−189.
(15) Xia, D. H.; Liu, H. D.; Xu, B. H.; Wang, Y. C. Single Ag atom engineered 3D-MnO2 porous hollow microspheres for rapid photo-thermocatalytic inactivation of E. coli under solar light. *Appl. Catal., B* **2019**, *245*, 177−189.
(16) Xia, D. H.; He, H. J.; Liu, H. D.; Wang, Y. C. Persulfate-mediated catalytic and photocatalytic bacterial inactivation by magnetic natural ilmenite. *Appl. Catal., B* **2018**, *238*, 70−81.
(17) Yang, J. L.; Huang, Y. J.; Chen, Y. W.; Xia, D. H. Active site-directed tandem catalysis on CuO/VO-MnO2 for efficient and stable catalytic ozonation of S-VOCs under mild condition. *Nano Today* **2020**, *35*, No. 100944.
(18) He, C.; Wang, Y. C.; Li, Z. Y.; Huang, Y. J. Facet Engineered #-MnO2 for Efficient Catalytic Ozonation of Odor CH3SH: Oxygen Vacancy-Induced Active Centers and Catalytic Mechanism. *Environ. Sci. Technol.* **2020**, *54*, 12771−12783.
(19) Hu, J. J.; Chen, Y. J.; Zhang, X. Z. Recent advances in nanomaterials for enhanced photothermal therapy of tumors. *Nanoscale* **2018**, *10*, 22657−22672.
(20) Wang, J.; Wu, X.; Shen, P.; Wang, J.; Shen, Y. D.; Shen, Y.; Webster, T. J.; Deng, J. J. Applications of Inorganic Nanomaterials in Photothermal Therapy Based on Combinational Cancer Treatment. *Int. J. Nanomed.* **2020**, *15*, 1903−1914.
(21) Civantos, F. J.; Karakullukcu, B.; Biel, M.; Silver, C. E.; Rinaldo, A.; Saba, N. F.; Takes, R. P.; Poorten, V. V.; Ferlito, A. A review of photodynamic therapy for neoplasms of the head and neck. *Adv. Ther.* **2018**, *35*, 324−340.
(22) Jung, H. S.; Verwilst, P.; Sharma, A.; Shin, J.; Sessler, J. L.; Kim, J. S. Organic molecule-based photothermal agents: an expanding photothermal therapy universe. *Chem. Soc. Rev.* **2018**, *47*, 2280−2297.
(23) Liu, J. M.; Chen, C. Y.; Zhao, Y. L. Progress and Prospects of Graphdiyne-Based Materials in Biomedical Applications. *Adv. Mater.* **2019**, *31*, No. 1804918.
(24) Chen, P. Y.; Ma, Y. C.; Zheng, Z.; Wu, C. F. Facile syntheses of conjugated polymers for photothermal tumour therapy. *Nat. Commun.* **2019**, *10*, No. 1192.
(25) Huang, X. H.; El-Sayed, I. H.; Qian, W.; El-Sayed, M. A. Cancer cell imaging and photothermal therapy in the near-infrared region by using gold nanorods. *J. Am. Chem. Soc.* **2006**, *128*, 2115−2120.
(26) Hao, C. L.; Gao, R.; Li, Y.; Xu, L. G. Chiral Semiconductor Nanoparticles for Protein Catalysis and Profiling. *Angew. Chem., Int. Ed.* **2019**, *58*, 7371−7374.
(27) Lal, S.; Clare, S. E.; Halas, N. J. Nanoshell-enabled photothermal cancer therapy: impending clinical impact. *Acc. Chem. Res.* **2008**, *41*, 1842−1851.
(28) Mattox, T. M.; Ye, X. C.; Manthiram, K.; Schuck, P. J.; Alivisatos, A. P. Chemical Control of Plasmons in Metal Chalcogenide and Metal Oxide Nanostructures. *Adv. Mater.* **2015**, *27*, 5830−5837.
(29) Li, Y. W.; Cheng, J. J.; Liu, Y. Z. Manipulation of Surface Plasmon Resonance in Sub-Stoichiometry Molybdenum Oxide Nanodots through Charge Carrier Control Technique. *J. Phys. Chem. C* **2017**, *121*, 5208−5214.
(30) Farahani, M. M.; Mollatayefeh, N. Chiral colloidal CdSe quantum dots functionalized with cysteine molecules: New optical nanosensor for selective detection and measurement of morphine. *Colloids Surf., A* **2019**, *569*, 78−84.
(31) Balfourier, A.; Luciani, N.; Wang, G.; Lelong, G.; Ersen, O.; Khelfa, A.; Alloyeau, D.; Gazeau, F.; Carn, F. Unexpected intracellular biodegradation and recrystallization of gold nanoparticles. *Proc. Natl. Acad. Sci. U.S.A.* **2020**, *117*, 103−113.
(32) Falagan-Lotsch, P. F.; Grzincic, E. M.; Murphy, C. J. One low-dose exposure of gold nanoparticles induces long-term changes in human cells. *Proc. Natl. Acad. Sci. U.S.A.* **2016**, *113*, 13318−13323.
(33) Osman, N. M.; Sexton, D. W.; Saleem, I. Y. Toxicological assessment of nanoparticle interactions with the pulmonary system. *Nanotoxicology* **2020**, *14*, 21−58.
(34) Wilhelm, S.; Tavares, A. J.; Dai, Q.; Ohta, S. J. Analysis of nanoparticle delivery to tumours. *Nat. Rev. Mater.* **2016**, *1*, No. 16014.
(35) Ballou, B.; Ernst, L. A.; Andreko, S.; Harper, T.; Fitzpatrick, J. A.; Waggoner, A. S.; Bruchez, M. P. Sentinel lymph node imaging using quantum dots in mouse tumor models. *Bioconjugate Chem.* **2007**, *18*, 389−396.
(36) Hao, J. L.; Song, G. S.; Liu, T.; Yi, X.; Yang, K.; Cheng, L.; Liu, Z. In vivo long-term biodistribution, excretion, and toxicology of PEGylated transition-metal dichalcogenides MS2 (M = Mo, W, Ti) nanosheets. *Adv. Sci.* **2017**, *4*, No. 1600160.
(37) Liu, T.; Chao, Y.; Gao, M.; Liang, C.; Chen, Q.; Song, G. S.; Cheng, L.; Liu, Z. Ultra-small MoS2 nanodots with rapid body clearance for photothermal cancer therapy. *Nano Res.* **2016**, *9*, 3003−3017.
(38) Zhang, X. D.; Zhang, J. X.; Wang, J. Y.; Yang, J.; Chen, J.; Shen, X.; Deng, J.; Deng, D. H.; Long, W.; Sun, Y. M.; Liu, C. L.; Li, M. X. Highly catalytic nanodots with renal clearance for radiation protection. *ACS Nano* **2016**, *10*, 4511−9.
(39) Mohamed, M. M.; Sloane, B. F. Cysteine cathepsins: multifunctional enzymes in cancer. *Nat. Rev. Cancer* **2006**, *6*, 764−775.
(40) Novotny, J. A.; Peterson, C. A. Molybdenum. *Adv. Nutr.* **2018**, *9*, 272−273.
(41) Jain, R. K.; Stylianopoulos, T. Delivering nanomedicine to solid tumors. *Nat. Rev. Clin. Oncol.* **2010**, *7*, 653−664.
(42) Shi, J. P.; LI, J.; Wang, Y.; Cheng, J. J.; Zhang, C. Y. Recent advances in MoS(2)-based photothermal therapy for cancer and infectious disease treatment. *J. Mater. Chem. B* **2020**, *8*, 5793−5807.
(43) Fakhri, A.; Nejad, P. A. Antimicrobial, antioxidant and cytotoxic effect of Molybdenum trioxide nanoparticles and application of this for degradation of ketamine under different light illumination. *J. Photochem. Photobiol., B* **2016**, *159*, 211−217.
(44) Liu, X. S.; Jiang, J. H.; Meng, H. Transcytosis—An effective targeting strategy that is complementary to "EPR effect" for pancreatic cancer nano drug delivery. *Theranostics* **2019**, *9*, 8018−8025.

https://doi.org/10.1021/acsomega.1c00101
ACS Omega 2021, 6, 11240−11247

(45) Jiang, S.; Chekini, M.; Qu, Z. B. Chiral Ceramic Nanoparticles of Tungsten Oxide and Peptide Catalysis. *J. Am. Chem. Soc.* **2017**, *139*, 13701−13712.
(46) Zu, H.; Guo, Y.; Yang, H.; Huang, D.; Liu, Z.; Liu, Y.; Hu, C. Rapid room-temperature preparation of MoO3x quantum dots by ultraviolet irradiation for photothermal treatment and glucose detection. *New J. Chem.* **2018**, *42*, 18533−18540.
(47) Yeom, J.; Santos, U. S.; Chekini, M.; Cha, M.; de Moura, A. F.; Kotov, N. A. Chiromagnetic NPs and Gels. *Science* **2018**, *359*, 309−314.
(48) Tian, M.; Li, F.; Hu, H. G.; Ma, J. T. Nano-Cu-Mediated Multi-Site Approach to Ultrafine MoO_2 Nanoparticles on Poly (diallyldimethylammonium chloride)- Decorated Reduced Graphene Oxide for Hydrogen Evolution Electrocatalysis. *ChemSusChem* **2019**, *12*, 441−448.
(49) Nie, R. F.; Shi, J. J.; Xia, S. X. MnO2/graphene oxide: a highly active catalyst for amide synthesis from alcohols and ammonia in aqueous media. *J. Mater. Chem.* **2012**, *22*, 18115−18118.
(50) Xu, J. T.; Gulzar, A.; Liu, Y. H.; Bi, H. T.; Gai, S. L.; Liu, B.; Yang, D.; He, F.; Yang, P. P. Integration of IR-808 Sensitized Upconversion Nanostructure and MoS2 Nanosheet for 808 nm NIR Light Triggered Phototherapy and Bioimaging. *Small* **2017**, *13*, No. 1701841.
(51) Hou, Z. Y.; Deng, K.; Li, C. X.; Deng, X. R.; Lian, H. Z.; Cheng, Z. Y.; Jin, D. Y.; Lin, J. 808 nm Light-triggered and hyaluronic acid-targeted dual-photosensitizers nanoplatform by fully utilizing Nd (3+)-sensitized upconversion emission with enhanced anti-tumor efficacy. *Biomaterials* **2016**, *101*, 32−46.
(52) Karimi, M.; Zangabad, P. S.; Baghaee, R. S.; Ghazadeh, M.; Mirshekari, H.; Hamblin, M. R. Smart Nanostructures for Cargo Delivery: Uncaging and Activating by Light. *J. Am. Chem. Soc.* **2017**, *139*, 4584−4610.
(53) Zhou, Z.; Wang, X. W.; Zhang, H.; Huang, H. X. Activating Layered Metal Oxide Nanomaterials via Structural Engineering as Biodegradable Nanoagents for Photothermal Cancer Therapy. *Small* **2021**, *17*, No. 2007486.
(54) Zhang, S. L.; Gao, H. J.; Bao, G. Physical Principles of Nanoparticle Cellular Endocytosis. *ACS Nano* **2015**, *9*, 8655−8671.
(55) Nusinow, D. P.; Szpyt, J.; Ghandi, M.; Rose, C. M.; McDonald, E. R., 3rd; Kalocsay, M.; Jané, VJ.; Gelfand, E.; Schweppe, D. K.; Jedrychowski, M.; Golji, J.; Porter, D. A.; Rejtar, T.; Wang, Y. K.; Kryukov, G. V.; Stegmeier, F.; Erickson, B. K.; Garraway, L. A.; Sellers, W. R.; Gygi, S. P. Quantitative Proteomics of the Cancer Cell Line Encyclopedia. *Cell* **2020**, *180*, 387−402.

https://doi.org/10.1021/acsomega.1c00101
ACS Omega 2021, 6, 11240−11247